Hybrid lanthanide nanoparticles as a new class of binary contrast agents with finely controlled longitudinal and transverse relaxivities for *in vivo* T_1/T_2 dual-weighted MRI and synergistic tumor diagnosis

Zhigao Yi, Zhenluan Xue, Xiaolong Li, Wei Lu, Hongrong Liu, Songjun Zeng, and Jianhua Hao**

Prof. S. J. Zeng, Z. G. Yi, Z. L. Xue, X. L. Li, Prof. H. R. Liu,
College of Physics and Information Science and Key Laboratory of Low-dimensional Quantum Structures and Quantum Control of the Ministry of Education, Hunan Normal University, Changsha, 410081, China.
E-mail: songjunz@hunnu.edu.cn
Z. G. Yi
School of Materials Science and Engineering, Key Laboratory of Low-dimensional Materials and Application Technology (Ministry of Education), Xiangtan University, Xiangtan, 411105, China.
Prof. J. H. Hao, Dr. W. Lu
Department of Applied Physics and Materials Research Center, The Hong Kong Polytechnic University, Hong Kong, China.
E-mail: jh.hao@polyu.edu.hk

Keywords: lanthanides nanoparticles, bioimaging agents, T_1/T_2 dual-weighted MRI, synergistic tumor diagnosis, relaxivities optimization

Magnetic resonance imaging (MRI), as one of most powerful and noninvasive diagnosis techniques in clinical and biomedical applications, has triggered intensive research interests in the early test of many diseases, which is ascribed to its high spatial resolution, noninvasive diagnostic manner, and no restriction of penetration based on the interaction of water protons with the surrounding molecules of tissues.[1] Signal intensity of MRI images can be enhanced by the introduction of appropriate contrast agents. MRI contrast agents are utilized to change relaxation rate of water protons and thereafter to realize the enhanced visualization effect between the focus of infection and the normal tissues. In MRI, there are two principal processes, namely longitudinal and transverse relaxation corresponding to T_1 recovery (spin-lattice) and T_2 decay (spin-spin), respectively. T_1 recovery causes positive (or bright) MRI

signal, while T_2 decay generates negative (or dark) images. The commonly used T_1 agents usually comprise paramagnetic complexes containing gadolinium (Gd^{3+}), iron (Fe^{3+}) or manganese (Mn^{2+}) ions.[2] However, these relatively small molecules generally have a short circulating time in vascular system within a few minutes because of their fast renal excretion, which is stumbling block to capture high-resolution MRI images. On the other hand, superparamagnetic iron oxide nanoparticles (SPIONs) have been used as T_2 weighted contrast enhancing agents owing to their freedom from strong magnetic interactions in dispersion and high stability under physiology conditions.[3] Nonetheless, the intrinsic disadvantages of SPIONs hinder their widespread clinical use, which include (1) diagnosis confusion between lesions labeled by T_2 agents and other low-level background areas, especially when the signal-to-noise ratio is low, (2) magnetic saturation within the normal range of external magnetic field strength in MRI scanners, and (3) potential toxicity ascribed to the possible Fenton reactions between Fe^{3+} and Fe^{2+} *in vivo*.[4]

Single T_1 or T_2 weighted MRI has its own unique merits and limitations, therefore the combination of the two modalities in MRI may provide more comprehensive and synergistic diagnostic information over the single modality.[3e,5,6] Furthermore, compared with other multi-modal imaging, the development of T_1/T_2 dual-weighted MRI strategies in a single instrumental system could efficiently eliminate from image matching difficulties resulting from reloading of samples, depth penetration, and spatial/time resolution of multiple imaging systems, and further improve the precision of diagnosis. Therefore, development of new-type and suitable dual-weighted contrast agents suffers an urgent demand. Some nanomaterials exhibit intrinsic T_1/T_2 contrast effects in dual-weighted MRI. Ultra-small SPIONs (about 3 nm in diameter) exhibit great potential as T_1 contrast agents, while the T_2 contrast effects are weak.[2d] In addition, the reported FeCo nanoparticles (NPs) system shows high T_1/T_2 contrast effects, but there is a lack of understanding the mechanism behind the observed effects.[3d] Gd^{3+}-labeled magnetite (Fe_3O_4) NPs or SPIONs were used as dual-contrast agents for T_1/T_2

dual-weighted MRI.[6] Unfortunately, the potential toxicity by leaked ions and aforementioned shortcomings of SPIONs limit their further biomedical use.

In spite of Gd^{3+} as T_1 agents, it is noticeable that other lanthanide ions (Ln^{3+}), e.g., Dy^{3+}, Ho^{3+}, Er^{3+}, Tm^{3+}, and Yb^{3+}, present relatively short transverse relaxation time, resulting in T_2 contrast effects.[7] While these Ln^{3+} ions are generally known for their upconversion luminescent properties, which provides strategies for designing multi-functional bioprobes in bioimaging, e.g., upconversion optical imaging, computed tomography (CT), MRI, etc.[8] Owing to the paramagnetic nature of Ln^{3+}, they do not distort the magnetic field and thus generate no magnetic susceptibility artifact.[4c] So far, Ln^{3+}-based nanomaterials have only been studied as contrast agent for single-weighted MRI. Unfortunately, limited works have focused on T_1/T_2 dual-contrast agents based on Ln-based nanomaterials. Recently, silica-coated core-shell upconversion nanostructures were employed as T_1/T_2 dual-weighted contrast agents, wherein both the longitudinal (r_1, $1/T_1$) and transverse (r_2, $1/T_1$) relaxivities have been optimized just via tuning the thickness of the silica shell.[9] However, the multiple synthesis and surface modification procedures increase the difficulties of precise control of particle size. Therefore, it is significantly important to develop a simple and facile strategy for synthesizing new and ideal T_1/T_2 dual-weighted contrast agents using Ln^{3+}. Hydrothermal reaction used herein is considered as facile and universal method in fabricating Ln^{3+}-doped NPs with well dispersity and narrow size distribution.[10] The relaxation proton majorly affects T_2 weighted MRI through a so-called Curie mechanism, which contributes to increase substantially with the external magnetic field and is proportional to the square of the effective magnetic moment of Ln^{3+}.[11] Doping other Ln^{3+} into Gd^{3+}-hosted NPs can efficiently change the transverse relaxivities, and as a result, can achieve the optimization of both the longitudinal and transverse relaxivities of NPs, as shown in **Figure 1a**.

In this work, we choose BaGd/LnF_5 (Ln^{3+} = Dy^{3+}, Er^{3+}, and Yb^{3+}) NPs as a proof of concept, because of the wide range of the magnetic moments of these selected ions (Dy^{3+}, μ_{eff}

= 10.63 μ_B, high; Er^{3+}, μ_{eff} = 9.59 μ_B, mediate; Yb^{3+}, μ_{eff} = 4.53 μ_B, low).[12] Oleate capping ligands of NPs are removed via a hydrochloric acid treatment to eliminate the quenching contribution from an inner-sphere mechanism.[8,13] To validate the synergistic enhanced contrast effects, these ligand-free NPs are applied in T_1/T_2 dual-weighted MRI and tumor diagnosis. This is the first time for demonstrating T_1/T_2 dual-weighted MRI and synergistic diagnosis of early-stage tumor using BaGd/ErF_5 NPs, which provides a general lanthanide doping method for constructing dual-modal T_1/T_2 probes in single host with tunable r_2/r_1 value. It should be mentioned that $BaGdF_5$:Yb, Er has proved to be an excellent upconversion fluorescent label in our previous studies.[8g] Combined with the report in this work, the hybrid lanthanide nanoparticles as multifunctional materials should be very useful in the area of multi-modal bioimaging.

BaGd/LnF_5 (Ln = Dy^{3+}, Er^{3+}, and Yb^{3+}) NPs were prepared via a hydrothermal method using oleic acid as capping ligands. The crystal phase of the as-prepared samples was revealed by XRD patterns. As depicted in Figure 1b, all of the position and intensity of the diffraction peaks of BaGd/LnF_5 (Ln^{3+} = Dy^{3+}, Er^{3+}, and Yb^{3+}) NPs were indexed to the standard pure cubic phase of $BaGdF_5$ (JCPDS No.: 24-0098), and there were no other impure diffraction peaks. Besides, in contrast to cubic phase of $BaGdF_5$, a little shift of diffraction peaks to higher angle direction was observed, which was due to the fact that the relative small ions, such as Dy^{3+} (1.167 Å), Er^{3+} (1.144 Å), or Yb^{3+} (1.125 Å), doped into Gd^{3+}-based (1.193 Å) host lattice.[14] Typical TEM images (Figure 1c-e) showed the near-spherical morphology and monodispersity of these Dy^{3+}, Er^{3+}, or Yb^{3+} doped $BaGdF_5$ NPs. Average diameters based on TEM results were calculated to be about 11, 15, and 14 nm for these BaGd/LnF_5 (Ln^{3+} = Dy^{3+}, Er^{3+}, and Yb^{3+}) NPs, respectively. High-resolution TEM images of these BaGd/LnF_5 (Ln^{3+} = Dy^{3+}, Er^{3+}, and Yb^{3+}) NPs (Figure S1a-c) show the measured interplanar distance of 2.86, 2.92, and 2.89 Å, respectively, which all corresponds to the (200) crystal plane of cubic phase of $BaGdF_5$, matching well with the XRD analysis aforementioned. Selected area electron

diffraction (SAED) patterns of these NPs (Figure S1d-f) present diffraction fringes of cubic phase, further confirming the above results from XRD.

To investigate the MRI performance of these single-phase BaGd/LnF_5 (Ln = Dy^{3+}, Er^{3+}, and Yb^{3+}) NPs, the hydrophobic NPs were converted to be hydrophilic ones using a diluted hydrochloric acid treatment,[15] and then their T_1 and T_2 relaxivity measurements as well as the corresponding phantom studies were conducted using a 1.5 T MRI system. The as-prepared samples solution with different Gd^{3+} or Ln^{3+} (Ln^{3+} = Dy^{3+}, Er^{3+}, and Yb^{3+}) concentrations were used for the measurement of r_1 and r_2 values based on the linear relationship of longitudinal and transverse relaxation rates versus concentrations of these magnetic mental ions. As performed in **Figure 2**a, the r_1 values are calculated to be 0.230, 0.219, and 0.145 mM^{-1} s^{-1} for Dy^{3+}, Er^{3+}, and Yb^{3+} doped $BaGdF_5$ NPs, respectively. The differences of r_1 values should mainly result from the different dopants, and the trend of change accords with the magnetic moment of the dopants. Actually, superparamagnetic T_2 contrast resource can easily generate an induced magnetic field under an external magnetic field, and as a result affect the electronic spin of paramagnetic T_1 contrast resource.[3e] The T_2 contrast resource increases the local magnetic field intensity of the T_1 contrast resource, and therefore making an enhancement of T_1 relaxation rates. Under identical conditions for other parameters, doping Dy^{3+} with the highest magnetic moment (μ_{eff} = 10.63 μ_B) has a greater impact on T_1 relaxation rates.

In contrast to longitude relaxivity, doping large amounts (50 wt%) of Dy^{3+}, Er^{3+}, or Yb^{3+} can more efficiently affect transverse relaxation rates of these contrast agents. As shown in Figure 2b, the r_2 values of BaGd/LnF_5 (Ln^{3+} = Dy^{3+}, Er^{3+}, and Yb^{3+}) NPs are measured to be 19.226, 6.634, and 2.861 mM^{-1} s^{-1}, respectively. As such, the r_2/r_1 value of BaGd/DyF_5 NPs is calculated to be 83.6 (Figure 2d), and the T_2 phantom images of which show the concentration-dependent negative contrast effects (Figure 2c). There is no obvious contrast changes in the corresponding T_1 phantom images. The r_2/r_1 values of BaGd/ErF_5 and

$BaGd/YbF_5$ NPs are calculated to be 30.3 and 19.7, respectively. Their *in vitro* T_1 or T_2 phantom images exhibit brighter or darker contrast signals with an increase in Ln^{3+} concentrations, indicating that these NPs could be emerged as synergistic dual-weighted MRI contrast agents. As control groups of experiment, the pure $BaGdF_5$, $BaDyF_5$, $BaErF_5$, and $BaYbF_5$ NPs are also synthesized for longitude and transverse relaxivities and dual-weighted *in vitro* MRI study, respectively. As shown in Figure S2, these un-doped NPs also present uniformed nanoparticle shape, single crystallinity of cubic phase, and high purity of components. The relaxivity time measurements (Figure S3) and the calculated r_2/r_1 values (Figure S4) of these pure NPs reveal that $BaGdF_5$ NPs can act as promising T_1 contrast agents owing to their low r_2/r_1 value (about 2.8). It is generally considered that the r_2/r_1 value, no exceeding 3, is suitable for acquiring positive contrast effects. However, the r_2/r_1 values of the pure $BaDyF_5$, $BaErF_5$, and $BaYbF_5$ NPs are calculated to be 334.8, 179.1, and 503.5, respectively, which are extremely high and indicate that all these three NPs should be promising T_2 contrast agents. We also conducted phantom images to validate the abilities of these pure NPs in T_1 and T_2 MRI. The *in vitro* MRI images (Figure S5) illustrate only T_1 contrast for $BaGdF_5$ NPs and only T_2 contrast for $BaDyF_5$, $BaErF_5$, and $BaYbF_5$ NPs, implying all these NPs can be used as single-weighted agents in MRI. Therefore, it is sufficiently effective to acquire synergistic contrast enhancement in T_1/T_2 dual-weighted MRI through the strategy of controlling longitude and transverse relaxivities via doping Ln^{3+} (Ln^{3+} = Dy^{3+}, Er^{3+}, and Yb^{3+}) into $BaGdF_5$ NPs.

Prior to applying these hybrid NPs to *in vivo* dual-weighted MRI, the cytotoxicity must be under consideration. The *in vitro* cytotoxicity of $BaGd/LnF_5$ (Ln^{3+} = Dy^{3+}, Er^{3+}, and Yb^{3+}) NPs on HeLa cells and HEK-293 cells were measured via MTT assays (**Figure 3**a). The viability of HeLa cells is above 85% when increasing the concentration of these NPs as high as 500 μg/mL. Besides, the viability of HEK-293 cells is not significantly affected by these NPs even as well at a relatively high dose at 500 μg/mL. The *in vitro* cell viability studies

reveal the low cytotoxicity of these BaGd/LnF_5 (Ln^{3+} = Dy^{3+}, Er^{3+}, and Yb^{3+}) NPs, indicating these NPs can be used as safe contrast agents for further *in vivo* bioimaging.

T_1/T_2 dual-weighted MRI has its great merits on improving diagnostic accuracy of disease through providing the comprehensive details of two modalities of images. Compared to the contrast effects of pure or other doped $BaGdF_5$ NPs, BaGd/ErF_5 NPs present high contrast abilities in T_1 and T_2 dual-weighted phantom images. Therefore, we choose BaGd/ErF_5 NPs for further dual-weighted *in vivo* MRI investigation. After intravenous injection of BaGd/ErF_5 NPs, T_1 and T_2 dual modality whole-body images of mice are captured using corresponding imaging sequences in a 1.5 T MRI system. As illustrated in **Figure 4**a, the liver region in the T_1 image after 1 h injection shows slight contrast enhancement when compared with the signal before administration. Besides, the positive contrast effects in the liver location are enlarged after 3 h injection of NPs. In addition, weak signal enhancement also occurs in the intestines and stomach regions after 1 and 3 h injection of NPs. During the T_1 MRI detection, T_2 images of the same mouse are also conducted using the same device. By contrast to the control image, the T_2 ones of the mouse present obviously darker contrast in the liver region after 1 and 3 h injection of NPs. Note that the positive and negative contrast enhancement of the mouse is a synergistic effect in the corresponding regions since the body of the animal is never moved during the whole imaging of the two modalities.

To further study the possible excrete mechanism as well as the feasibility of tumor detection of BaGd/ErF_5 NPs, groups of tumor (HeLa cells) bearing mice under injection of NPs from tail vein are used for dual-weighted *in vivo* MRI, the coronal images of which in different tissue sections are shown in **Figure 5**. Seen from the left panel in Figure 5a, the intense positive contrast enhancements are presented in the intestines and stomach regions after 3 h injection of NPs, while the corresponding tissues in the image before injection exhibit an indistinguishable state. The same regions in the T_2 weighted image (left panel in Figure 5b) after injection show darker contrast effects over the image captured before

injection, especially in the stomach location. Besides, sharp bright and dark contrast effects are also presented in the liver region (middle panel in Figure 5) in the corresponding modalities. It is noted that the injection of these BaGd/ErF_5 NPs can greatly enhance the visualization of the hepatic portal vein under T_2 weighted *in vivo* MRI. This phenomenon is mainly ascribed to the high accumulation of NPs and the resulting dark contrast enhancement in the liver parenchyma, leading to the convenient visualization of the vessel. These synergetic imaging results are matched well with the former analysis in the normal mice. More significantly, the signal intensity of the tumor site in both T_1 and T_2 weighted MRI has changed. In T_1 weighted MRI, the outline of the tumor is clear and the brightness is obviously higher than the image before injection (middle panel in Figure 5a). The signal intensity in a different transverse section of the tumor also present the trend of increase after injection. By contrast, the tumor site shows the bright image initially and then becomes dark after injection of NPs in T_2 weighted MRI. Therefore, the obtained BaGd/ErF_5 NPs can be used as high-contrast and dual-modal agents in both T_1 and T_2 weighted MRI, the synergistic imaging effects of which can provide more details of the lesion, and as a result, improve the diagnostic accuracy of cancer.

Except for dual-weighted MRI contrast functionality, these BaGd/ErF_5 NPs containing high-*Z* elements (e.g., Ba, Gd, and Er) exhibit novel capability of X-ray absorption, implying their additional application in X-ray CT bioimaging.[8g,16] To verify the CT contrast efficiency of BaGd/ErF_5 NPs, groups of normal Kunming mice are intravenously injected and detected using a micro-CT system. From the 3D renderings of *in vivo* CT images (Figure S6a), there is no signal in organs before injection of NPs. However, obvious CT contrast effects in the liver region are observed after 3 h injection of NPs from tail vein (Figure S6b). These finding indicates that our developed BaGd/ErF_5 NPs can emerge as multifunctional contrast agents for not only synergistic dual-weighted T1/T2 MRI but CT bioimaging.

In summary, we have demonstrated that the longitudinal and transverse relaxivities of NPs can be precisely controlled via a simple and efficient strategy that single doping Ln^{3+} (Ln^{3+} = Dy^{3+}, Er^{3+}, and Yb^{3+} here) into $BaGdF_5$ host traditionally used for upconversion fluorescence bioimaging for the first time. The obtained $BaGd/ErF_5$ NPs present simultaneously excellent T_1 and T_2 contrast effects in the phantom images, which should be a new class of dual-contrast agents for T_1/T_2 dual-weighted MRI. The low cytotoxicity of these NPs can be validated by MTT assays using HeLa cells and HEK-293 cells. The synergistic contrast enhancement of tissues in the live mice using $BaGd/ErF_5$ NPs can be realized by T_1/T_2 dual-weighted MRI *in vivo*. Moreover, visualization of tumor can be also synergistically enhanced in both T_1/T_2 weighted *in vivo* MRI based on the EPR effect. Therefore, $BaGd/ErF_5$ NPs synthesized in this work can be emerged as synergistic contrast enhancing agents in T_1/T_2 dual-weighted MRI, as well as used as promising diagnostic agents of cancer. These findings provide a platform for designing synergistic T_1/T_2 dual-modal MRI agents to improve diagnostic accuracy by a general Ln^{3+}-doping method.

Experimental Section

Chemicals and materials: All reagents were of analytical purity and used without further purification. $LnCl_3 \cdot 6H_2O$ (99.99%, Ln^{3+} = Dy^{3+}, Er^{3+}, Yb^{3+}, and Gd^{3+}), and oleic acid (OA) were purchased from Sigma-Aldrich. $BaCl_2$, NaOH, and NH_4F and other regents were bought from Sinopharm Chemical Reagent Co., China.

Synthesis of OA-capped NPs: $BaGd/LnF_5$ (Ln^{3+} = Dy^{3+}, Er^{3+}, and Yb^{3+}) NPs were prepared by a hydrothermal method utilizing OA as stabilizing agents. In a typical process,[9] 1.5 mL of NaOH solution (0.4g/mL) was mixed with 10 mL of ethanol followed by addition with 20 mL of OA. After forming a transparent homogeneous mixture, 1 mL of $BaCl_2$ solution (1.0 M) and total amounts (1 mmol) of $GdCl_3$ and $LnCl_3$ (Ln^{3+} = Dy^{3+}, Er^{3+}, and Yb^{3+}) were added in the above solution. After that, 6 mL of NH_4F aqueous solution (1.0 M) was added slowly. All

these processes aforementioned were under vigorous stirring. After 30 min agitation, the obtained mixture was transferred into a 50 mL stainless Teflon-lined autoclave. The reaction system was sealed and maintained at 200 °C for 24 h. After reaction, the system was cooled to room temperature naturally. The samples were separated by centrifugation and washed with ethanol and de-ionized (DI) water in sequence for several times. Products were dried in air at 60 °C for a whole day.

Synthesis of ligand-free NPs: For animal experiments based on these NPs, OA-capped NPs were converted to hydrophilic one using a HCl treated method. In a typical method,[15] 100 mg of OA-capped NPs was added into 20 mL of DI water. The solution was then under agitation for 2 h after tuning the pH value at 4 using dilute HCl solution. As a consequence, the carboxylate groups of the oleate ligand were removed. And then, two layers (ether and water layers) were formed by adding diethyl ether into the clarified solution and oleic acid in water layer was completely extracted for several times. Ligand-free NPs were then precipitated in acetone and collected by centrifugation and finally dispersed in DI water and used as contrast agents for further biomedical investigation.

Characterization: X-ray diffraction (XRD) pattern of OA-capped NPs were measured by a D/max-yA system X-ray diffractometer at 40 kV and 250 mA with Cu-Ka radiation - = 1.54056 Å). The microstructure of OA-capped and ligand-free NPs were demonstrated by TEM, SAED, and HR-TEM via a JEM-2100F TEM equipped with an Oxford Instrument EDS system using an accelerating voltage of 200 kV.

Cytotoxicity assay: The cell cytotoxicity *in vitro* of these ligand-free NPs in HeLa cells was measured via a 3-(4,5-dimethylthiazol-2-yl)-2,5 diphenyl-tetrazolium bromide (MTT) proliferation assay method. HeLa cells were cultured in Dulbecco's Modified Eagle Medium (DMEM) containing 10% fetal bovine serum, 1% penicillin and streptomycin at 37 °C and with 5% CO_2. Hela cells were transferred into a 96-well cell culture plate at 10^6 per well and incubated at 37 °C and with 5% CO_2 atmosphere for 24 h. Ligand-free NPs with different

concentration (0, 50, 100, 250, and 500 μg/mL) were added into the wells in the absence of serum. Microscope observation was executed after another 4 h incubation of the wells at 37 °C and with 5% CO_2. Cell viability was calculated by a typical MTT assy. The procedures of MTT assay using HEK-293 cells are similar with the ones using Hela cells.

T_1/T_2 dual-weighted MRI in vitro: *In vitro* dual-weighted MRI images were acquired using a 1.5 T MRI system (HT-ANNMR-50, Shanghai Shinning Global Scientific and Educational Equipment Co.). Aqueous solutions containing ligand-free NPs with well-designed Gd^{3+} as well as Dy^{3+}/Er^{3+}/Yb^{3+} concentrations were transferred into 1.0 mL tubes for dual-weighted MRI. T_1-weighted sequence was performed as follows: Spin Echo (SE), Time of Repetition (TR) = 100 ms, Time of Echo (TE) = 10.6 ms, Matrix = 512 × 256, Field of View (FOV) = 50 × 130, Slice Thickness (ST) = 0.5 mm. T_2-weighted sequence was performed as follows: SE, TR = 500 ms, TE = 65 ms, matrix = 512 × 256, FOV = 50 × 130, ST = 0.5 mm. Relaxivity values (r_1 or r_2) were calculated using the linear fitting of $1/T_1$ or $1/T_2$ relaxation times as a function of Gd^{3+} or Dy^{3+}/Er^{3+}/Yb^{3+} concentration, respectively.

Synergistic T_1/T_2 dual-weighted MRI in vivo: All animal procedures were in agreement with the institutional animal use and care regulations approved by the Laboratory Animal Center of Hunan. *In vivo* T_1 and T_2 dual-weighted MRI were conducted on a 1.0 T MRI scanner (Aspect Imaging, M3 MRI system) and their images were captured before and after administration of these hydrophilic NPs at different time points. Briefly, Kunming mice were firstly anesthetized via intraperitoneal injection with 150 μL of pentobarbital sodium aqueous solution 10 wt%) and then intravenously injected with 50 μL of ligand-free NPs aqueous solution (1.2 mM Gd^{3+} concentration). Synergistic *in vivo* bioimaging based on T_1 and T_2 dual-weighted MRI were also performed by using the T_1 and T_2 weighted sequences aforementioned, respectively, and their coronal cross-sectional images were captured before and after 30 min and 3 h intravenous injection of NPs.

Synergistic detection of tumor via in vivo T_1/T_2 dual-weighted MRI: To further validate the dual-weighted high-contrast capabilities of these hydrophilic NPs, the tumor-bearing mice models were established for synergistic detection of tumor using T_1 and T_2 dual-weighted MRI. HeLa cells (1×10^7) were suspended in 50 μL of phosphate buffer saline solution and implanted into BALB/C mice by subcutaneous injection. *In vivo* tumor imaging was performed using the implanted mice after two weeks rearing under germ-free conditions. The inoculated tumor modals were intraperitoneally injected 150 μL of pentobarbital sodium aqueous solution (10 wt%) and then intravenously injected 50 μL of ligand-free NPs aqueous solution (1.2 mM Gd^{3+} concentration) from tail vein. Synergistic detection of tumor utilizing T_1 and T_2 dual-weighted MRI modalities were captured before and after 3 h intravenous injection of NPs.

In vivo CT bioimaging: To investigate the feasibilities of these hydrophilic NPs for CT imaging function, a proof-of-concept experiment was conducted using a micro-CT (Hitachi Aloka Medical, Latheta LCT-200). Groups of mice were anesthetized via intraperitoneal injection with 150 μL of pentobarbital sodium 10 wt%) and intravenously injected with 200 μL of ligand-free NPs aqueous solution (30 mg/mL) from tail vein. *In vivo* CT imaging was measured before and after 3 hours intravenous injection of NPs. *In vivo* CT images were captured using the following parameters: 80 kVp; 0.5 mA; Base Resolution, 80 x 80 μm^2; Scanning Thickness, 80 μm. The two-dimensional cross-sectional images were directly captured by the device and the corresponding 3D renderings were constructed by VGStudio MAX 2.2 Software.

Supporting Information

Supporting Information is available from the Wiley Online Library or from the author.

Acknowledgements

This work was supported by the National Natural Science Foundation of China (Nos. 51102202), specialized research Fund for the Doctoral Program of Higher Education of China (No. 20114301120006) and Hunan Provincial Natural Science Foundation of China (Nos. 12JJ4056 and 13JJ1017), and Scientific Research Fund of Hunan Provincial Education Department (13B062). We thank Dr. Hui Hui and Mr Xiao Liang in Key Laboratory of molecular Imaging, Chinese Academy of Sciences for *in vivo* MRI and helpful discussions.

Received: ((will be filled in by the editorial staff))
Revised: ((will be filled in by the editorial staff))
Published online: ((will be filled in by the editorial staff))

[1] a) R. Weissleder, M. J. Pittet, *Nature* **2008**, *452*, 580; b) J. S. Ananta1, B. Godin, R. Sethi, L. Moriggi, X. W. Liu, R. E. Serda, R. Krishnamurthy, R. Muthupillai, R. D. Bolskar, L. Helm, M. Ferrari, L. J. Wilson, P. Decuzzi, *Nat. Nanotech.* **2010**, *5*, 815; c) G. K. Das, N. J. J. Johnson, J. Cramen, B. Blasiak, P. Latta, B. Tomanek, F. C. J. M. van Veggel, *J. Phys. Chem. Lett.* **2012**, *3*, 524; d) R. Kumar, M. Nyk, T. Y. Ohulchanskyy, C. A. Flask, P. N. Prasad, *Adv. Funct. Mater.* **2009**, *19*, 853; e) Z. H. Zhao, X. M. Wang, Z. J. Zhang, H. Zhang, H. Y. Liu, X. L. Zhu, H. Li, X. Q. Chi, Z. Y. Yin, J. H. Gao, *ACS Nano* **2015**, *9*, 2749; f) Y. J. Chen, H. C. Gu, D. S. Zhang, F. Li, T. Y. Liu, W. L. Xia, *Biomaterials* **2014**, *35*, 10058; g) R. P. Mason, D. Zhao, J. Pacheco-Torres, W. Cui, V. D. Kodibagkar, P. K. Gulaka, G. Hao, P. Thorpe, E. W. Hahn, P. Peschke, *Q. J. Nucl. Med. Mol. Imaging* **2010**, *54*, 259.

[2] a) M. Bottrill, L. Kwok, N. J. Long, *Chem. Soc. Rev.* **2006**, *35*, 557; b) K. N. Raymond, V. C. Pierre, *Bioconjug Chem.* **2004**, *16*, 3; c) J. S. Kim, W. J. Rieter, K. M. L. Taylor, H. Y. An, W. L. Lin, W. B. Lin, *J. Am. Chem. Soc.* **2007**, *129*, 8962; d) B. H. Kim, N. Lee, H. Kim, K. An, Y. I. Park, Y. Choi, K. Shin, Y. Lee, S. G. Kwon, H. B. Na, J. G. Park, T. Y. Ahn, Y. W. Kim, W. K. Moon, S. H. Choi, T. Hyeon, *J. Am. Chem. Soc.* **2011**, *133*, 12624; e) U. I. Tromsdorf, O. T. Bruns, S. C. Salmen, U. Beisiegel, H. Weller, *Nano Lett.* **2009**, *9*, 4434; f) F. Q. Hu, Q. J. Jia, Y. L. Li, M. Y. Gao, *Nanotechnology* **2011**, *22*, 245604; g) H. B. Na, J. H. Lee, K. An, Y. I. Park, M. Park, I. S. Lee, D. H. Nam, S. T. Kim, S. H. Kim, S. W. Kim, K. H. Lim, K. S. Kim, S. O. Kim, T. Hyeon, *Angew. Chem. Int. Ed.* **2007**, *46*, 5397; h)

H. Yang, Y. M. Zhuang, H. Hu, X. X. Du, C. X. Zhang, X. Y. Shi, H. X. Wu, S. P. Yang, *Adv. Funct. Mater.* **2010**, *20*, 1733; i) T. Kim, E. Momin, J. Choi, K. Yuan, H. Zaidi, J. Kim, M. Park, N. Lee, M. T. McMahon, A. Quinones-Hinojosa, J. W. M. Bulte, T. Hyeon, A. A. Gilad, *J. Am. Chem. Soc.* **2011**, *133*, 2955.

[3] a) Y. W. Jun, J. H. Lee, J. Cheon, *Angew. Chem. Int. Ed.* **2008**, *47*, 5122; b) J. Park, K. An, Y. Hwang, J. G. Park, H. J. Noh, J. Y. Kim, J. H. Park, N. M. Hwang, T. Hyeon, *Nat. Mater.* **2004**, *3*, 891; c) J. H. Lee, Y. M. Huh, Y. W. Jun, J. W. Seo, J. T. Jang, H. T. Song, S. Kim, E. J. Cho, H. G. Yoon, J. S. Suh, J. Cheon, *Nat. Med.* **2007**, *13*, 95; d) W. S. Seo, J. H. Lee, X. Sun, Y. Suzuki, D. Mann, Z. Liu, M. Terashima, P. C. Yang, M. V. McConnell, D. G. Nishimura, H. Dai, *Nat. Mater.* **2006**, *5*, 971; e) Z. J. Zhou, D. T. Huang, J. F. Bao, Q. L. Chen, G. Liu, Z. Chen, X. Y. Chen, J. H. Gao, *Adv. Mater.* **2012**, *24*, 6223; f) W. C. Xiao, J. Lin, M. L. Li, Y. J. Ma, Y. X. Chen, C. F. Zhang, D. Li, H. C. Gu, *Contrast Media. Mol. I.* **2012**, *7*, 320.

[4] a) M. Valko, H. Morris, M. T. D. Cronin, *Curr. Med. Chem.* **2005**, *12*, 1161; b) K. Jellinger, W. Paulus, I. Grundke-Iqbal, P. Riederer, M. B. H. Youdim, *J. Neural Transm.* **1990**, *2*, 327; c) H. B. Na, I. C. Song, T. Hyeon, *Adv. Mater.* **2009**, *21*, 2133; d) J. W. M. Bulte, D. L. Kraitchman, NMR Biomed. 2004, 17, 484.

[5] a) J. S. Choi, J. H. Lee, T. H. Shin, H. K. Song, E. Y. Kim, J. Cheon, *J. Am. Chem. Soc.* **2010**, *132*, 11015; b) G. H. Im, S. M. Kim, D. G. Lee, W. J. Lee, J. H. Lee, I. S. Lee, *Biomaterials* **2013**, *34*, 2069; c) H. Y. Chen, B. Qi, T. Moore, D. C. Colvin, T. Crawford, J. C. Gore, F. Alexis, O. T. Mefford, J. N. Anker, *Small* **2014**, *10*, 160; d) J. Chen, W. J. Zhang, Z. Guo, H. B. Wang, D. D. Wang, J. J. Zhou, Q. W. Chen, *ACS Appl. Mater. Interfaces* **2015**, *7*, 5373; e) L. J. Yang, Z. J. Zhou, H. Y. Liu, C. Q. Wu, H. Zhang, G. M. Huang, H. Ai, J. H. Gao, *Nanoscale*, **2015**, *7*, 6843.

[6] a) Z. J. Zhou, C. Q. Wu, H. Y. Liu, X. L. Zhu, Z. H. Zhao, L. R. Wang, Y. Xu, H. Ai, J. H. Gao, *ACS Nano* **2015**, *9*, 3012; b) H. Yang, Y. M. Zhuang, Y. Sun, A. T. Dai, X. Y. Shi,

D. M. Wu, F. Y. Li, H. Hu, S. P. Yang, *Biomaterials* **2011**, *32*, 4584; c) K. Cheng, M. Yang, R. P. Zhang, C. X. Qin, X. H. Su, Z. Cheng, *ACS Nano* **2014**, *8*, 9884; d) K. H. Bae, Y. B. Kim, Y. Lee, J. Hwang, H. Park, T. G. Park, *Bioconjug Chem.* **2010**, *21*, 505; e) X. Y. Wang, Z. J. Zhou, Z. Y. Wang, Y. X. Xue, Y. Zeng, J. H. Gao, L. Zhu, X. Z. Zhang, G. Liu, X. Y. Chen, *Nanoscale*, **2013**, *5*, 8098.

[7] a) D. L. Ni, W. B. Bu, S. J. Zhang, X. P. Zheng, M. Li, H. Y. Xing, Q. F. Xiao, Y. Y. Liu, Y. Q. Hua, L. P. Zhou, W. J. Peng, K. L. Zhao, J. L. Shi, *Adv. Funct. Mater.* **2014**, *24*, 6613; b) I. Bertini, F. Capozzi, C. Luchinat, G. Nicastro, Z. C. Xia, *J. Phys. Chem.* **1993**, *97*, 6351; c) K. Kattel, J. Y. Park, W. Xu, H. G. Kim, E. J. Lee, B. A. Bony, W. C. Heo, J. J. Lee, S. Jin, J. S. Baeck, Y. Chang, T. J. Kim, J. E. Bae, K. S. Chae, G. H. Lee, *ACS Appl. Mater. Interfaces* **2011**, *3*, 3325; d) M.K. Tsang, G. Bai, J. Hao, *Chem. Soc. Rev.* **2015**, *44*, 1585.

[8] a) F. Wang, X. G. Liu, *Chem. Soc. Rev.* **2009**, *38*, 976; b) J. Zhou, Z. Liu, F. Y. Li, *Chem. Soc. Rev.* **2012**, *41*, 1323; c) N. M. Idris, M. K. Gnanasammandhan, J. Zhang, P. C. Ho, R. Mahendran, Y. Zhang, *Nature Medicine* **2012**, *18*, 1580; d) L. Cheng, C. Wang, L. Z. Feng, K. Yang, Z. Liu, *Chem. Rev.* **2014**, *114*, 10869; e) D. M. Yang, P. A. Ma, Z. Y. Hou, Z. Y. Cheng, C. X. Li, J. Lin, *Chem. Soc. Rev.* **2015**, *44*, 1416; f) G. Tian, Z. J. Gu, L. J. Zhou, W. Y. Yin, X. X. Liu, L. Yan, S. Jin, W. L. Ren, G. M. Xing, S. J. Li, Y. L. Zhao, *Adv. Mater.* **2012**, *24*, 1226; g) S. J. Zeng, M. K. Tsang, C. F. Chan, K. L. Wong, J. H. Hao, *Biomaterials* **2012**, *33*, 9232; h) L. Zhou, R. Wang, C. Yao, X. M. Li, C. L. Wang, X. Y. Zhang, C. J. Xu, A. J. Zeng, D. Y. Zhao, F. Zhang, *Nat. Commun.* **2015**, *6*, 6938.

[9] F. Chen, W. B. Bu, S. J. Zhang, J. N. Liu, W. P. Fan, L. P. Zhou, W. J. Peng, J. L. Shi, *Adv. Funct. Mater.* **2013**, *23*, 298.

[10] a) F. Wang, Y. Han, C. S. Lim, Y. H. Lu, J. Wang, J. Xu, H. Y. Chen, C. Zhang, M. H. Hong and X. G. Liu, *Nature* **2010**, *463*, 1061; b) Z. G. Yi, W. Lu, H. R. Liu, S. J. Zeng, *Nanoscale*, **2015**, *7*, 542; c) S. J. Zeng, Z. G. Yi, W. Lu, C. Qian, H. B. Wang, L. Rao, T. M. Zeng, H. R. Liu, H. J. Liu, B. Fei, J. H. Hao, *Adv. Funct. Mater.* **2014**, *24*, 4196.

[11] L. Vander Elst, A. Roch, P. Gillis, S. Laurent, F. Botteman, J. W. Bulte, R. N. Muller, *Magn. Reson. Med.* **2002**, *47*, 1121.

[12] a) Z. Kovacs, K. N. Green, S. J. Ratnakar, A. D. Sherry, *Chem. Rev.* **2010**, *110*, 2960; b) M. Norek, J. A. Peters, *Prog. Nucl. Magn. Reson. Spectrosc.* **2011**, *59*, 64.

[13] P. Caravan, J. J. Ellison, T. J. McMurry, R. B. Lauffer, *Chem. Rev.* **1999**, *99*, 2293.

[14] R. D. Shannon, *Acta Cryst.* **1976**, *A32*.

[15] N. Bogdan, Vetrone, G. A. Ozin, J. A. Capobianco, *Nano Lett.* **2011**, *11*, 835.

[16] a) S. Yu, A. Watson, *Chem. Rev.* 1999, *99*, 2353; b) Y. Y. Liu, K. L. Ai, J. H. Liu, Q. H. Yuan, Y. Y. He, L. H. Lu, *Angew. Chem. Int. Ed.* **2012**, *51*, 1437; c) Z. G. Yi, W. Lu, Y. R. Xu, J. Yang, L. Deng, C. Qian, T. M. Zeng, H. B. Wang, L. Rao, H. R. Liu, S. J. Zeng, *Biomaterials* **2014**, *35*, 9689.

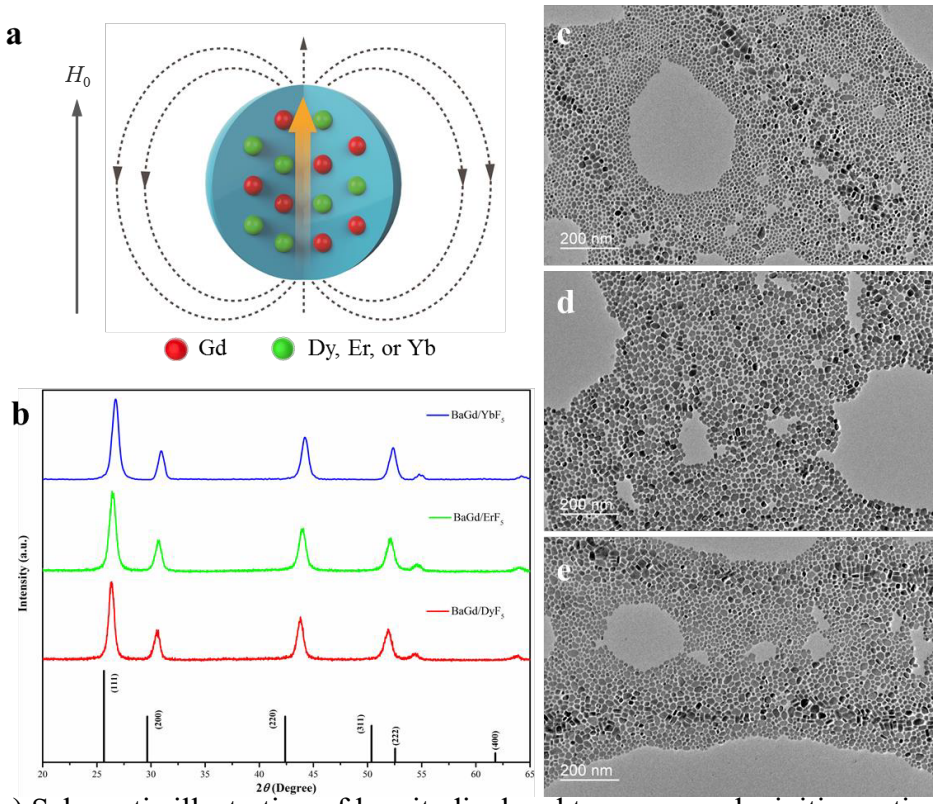

Figure 1. (a) Schematic illustration of longitudinal and transverse relaxivities optimization of the T_1/T_2 dual-weighted MRI contrast agents via doping Ln^{3+} (Ln = Dy^{3+}, Er^{3+}, and Yb^{3+}) into Gd^{3+} based host. (b) XRD patterns and standard card of cubic phase $BaGdF_5$ crystal (JCPDS file No. 24-0098). (c-e) Corresponding the Dy^{3+}, Er^{3+}, or Yb^{3+} doped $BaGdF_5$ NPs, respectively.

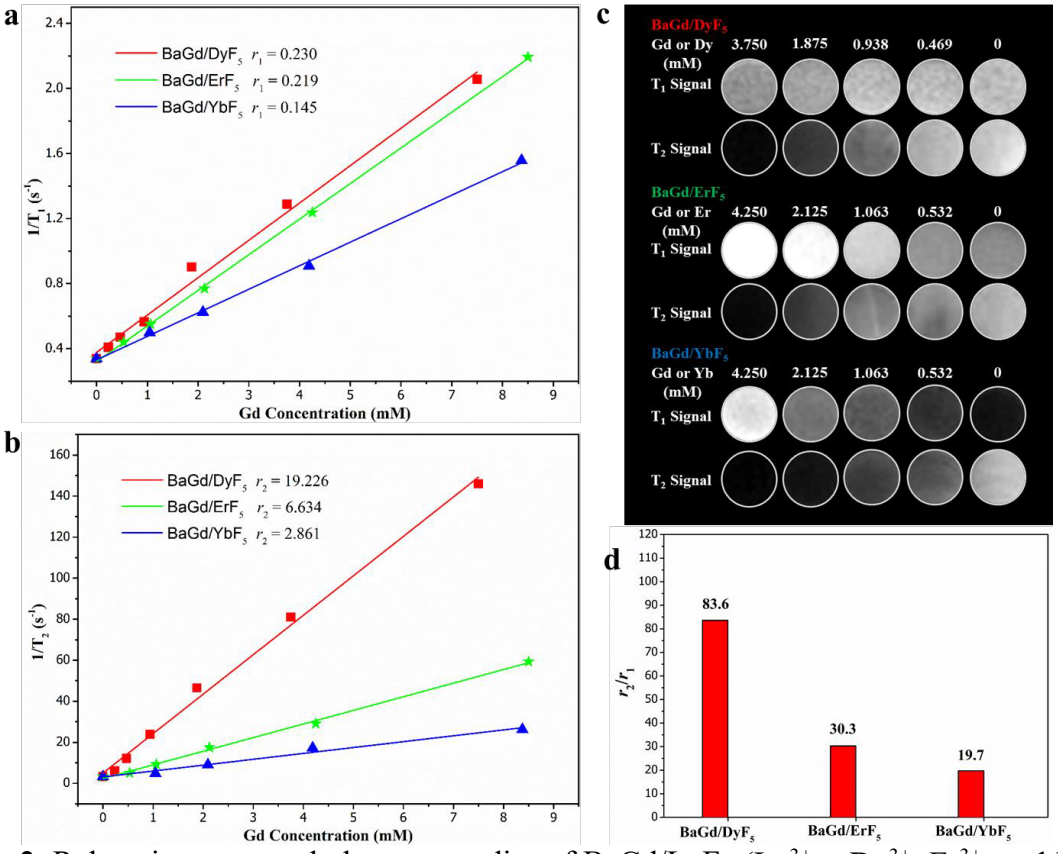

Figure 2. Relaxation rates and phantom studies of $BaGd/LnF_5$ (Ln^{3+} = Dy^{3+}, Er^{3+}, and Yb^{3+}) NPs. (a) and (b) the measured r_1 and r_2 values according to longitude and transverse relaxation rates versus Gd^{3+} concentration, respectively; (c) *in vitro* T_1 and T_2 phantom images of NPs; (d) the calculated r_2/r_2 values of these NPs.

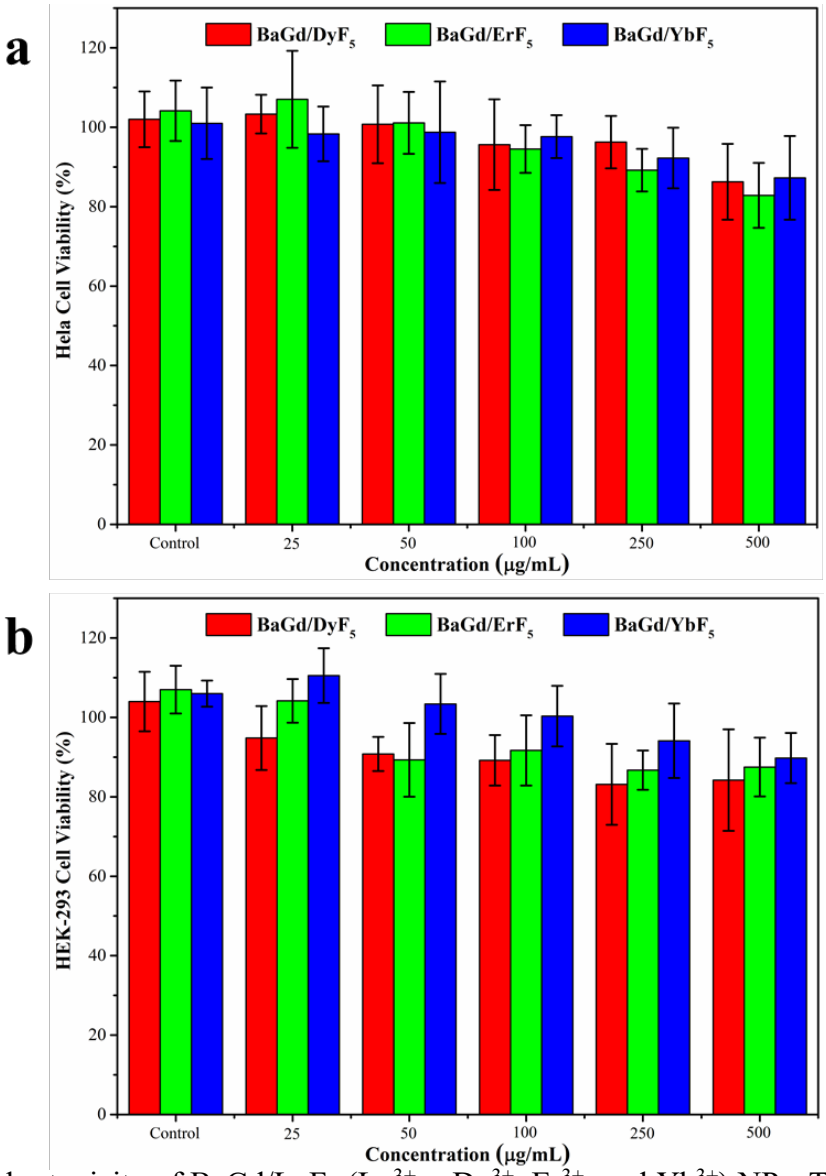

Figure 3. Cellular toxicity of BaGd/LnF_5 (Ln^{3+} = Dy^{3+}, Er^{3+}, and Yb^{3+}) NPs. The viability of (a) Hela cells and (b) HEK-293 cells after treatment of various concentration of corresponding NPs.

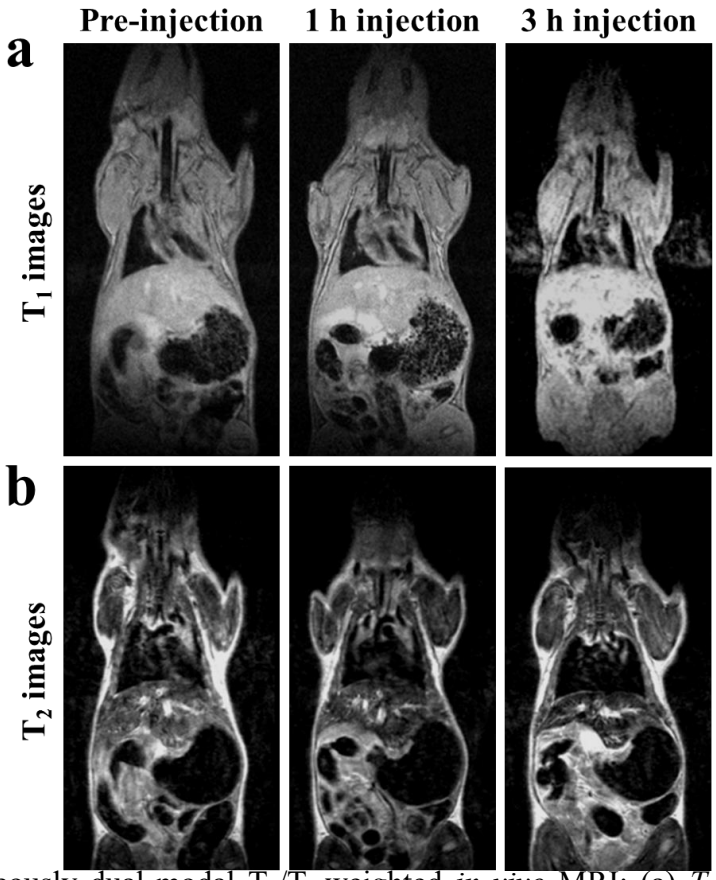

Figure 4. Simultaneously dual-modal T_1/T_2 weighted *in vivo* MRI: (a) T_1 and (b) T_2 MRI coronal images of a normal mouse before as well as after 1 and 3 hours intravenous injection of BaGd/ErF_5 NPs from tail vein.

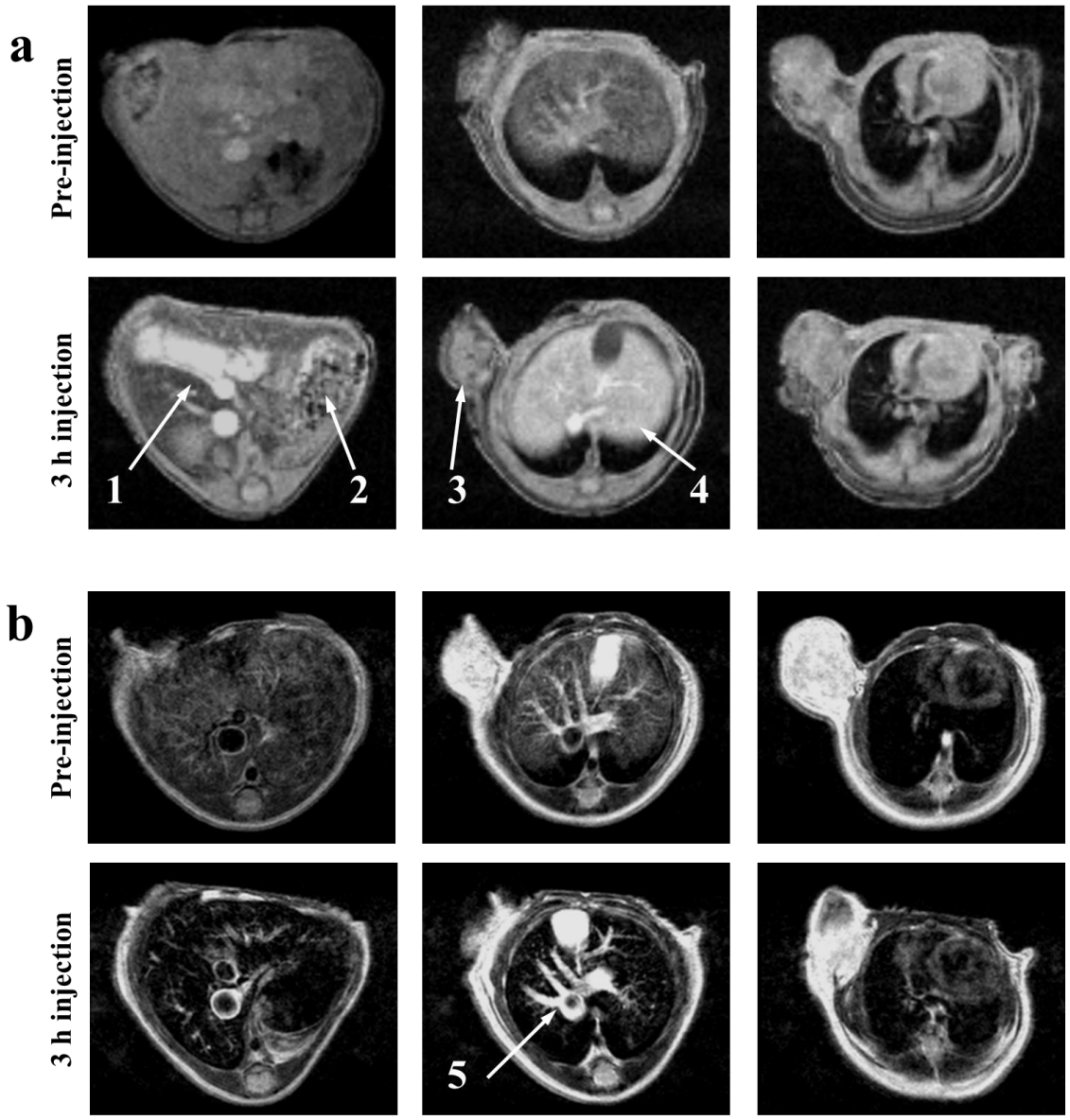

Figure 5. Synergistic *in vivo* dual-modal T_1/T_2 guided tumor diagnosis: (a) T_1 and (b) T_2 weighted MRI transverse images of a tumor-bearing mouse before and 3 hours intravenous injection of $BaGd/ErF_5$ NPs from tail vein. The digital number refers to the corresponding organs with enhanced contrast effects, such as, 1: Intestines, 2: Stomach, 3: Tumor, 4: Liver, 5: Portal vein.

A new type of hybrid lanthanide nanoparticles have been reported as binary contrast agents in dual-weighted T_1/T_2 MRI and synergistic tumor diagnosis. The longitude and transverse relaxivities of these developed nanoparticles can be precisely controlled by tuning dopants, providing a strategy and platform for designing simultaneous T_1/T_2 enhancing agents.

Keyword: lanthanides nanoparticles, bioimaging agents, dual-weighted T_1/T_2 MRI, synergistic tumor diagnosis, relaxivities optimization

Z. G. Yi, Z. L. Xue, X. L. Li, W. Lu, H. R. Liu, S. J. Zeng,* and J. H. Hao*

Hybrid lanthanide nanoparticles as a new class of binary contrast agents with finely controlled longitudinal and transverse relaxivities for *in vivo* T_1/T_2 dual-weighted MRI and synergistic tumor diagnosis

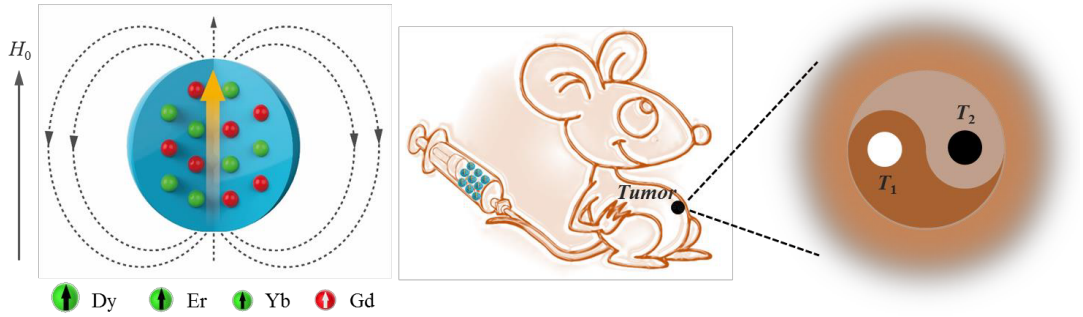

Supporting Information

Hybrid lanthanide nanoparticles as new class of binary contrast agents with finely controlled longitudinal and transverse relaxivities for *in vivo* T_1/T_2 dual-weighted MRI and synergistic tumor diagnosis

Zhigao Yi, Zhenluan Xue, Xiaolong Li, Wei Lu, Hongrong Liu, Songjun Zeng, and Jianhua Hao**

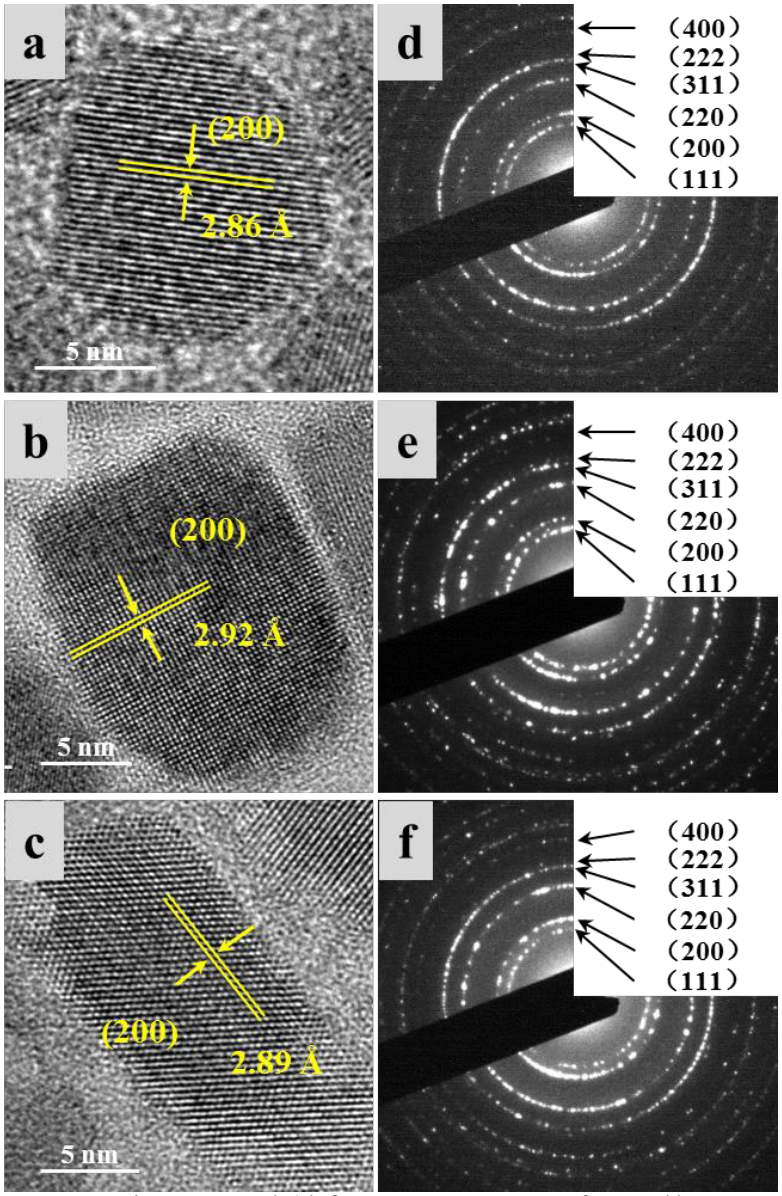

Figure S1. (a-c) HR-TEM images and (d-f) SAED patterns of BaGd/LnF_5 NPs (Ln^{3+} = Dy^{3+}, Er^{3+}, and Yb^{3+}), respectively.

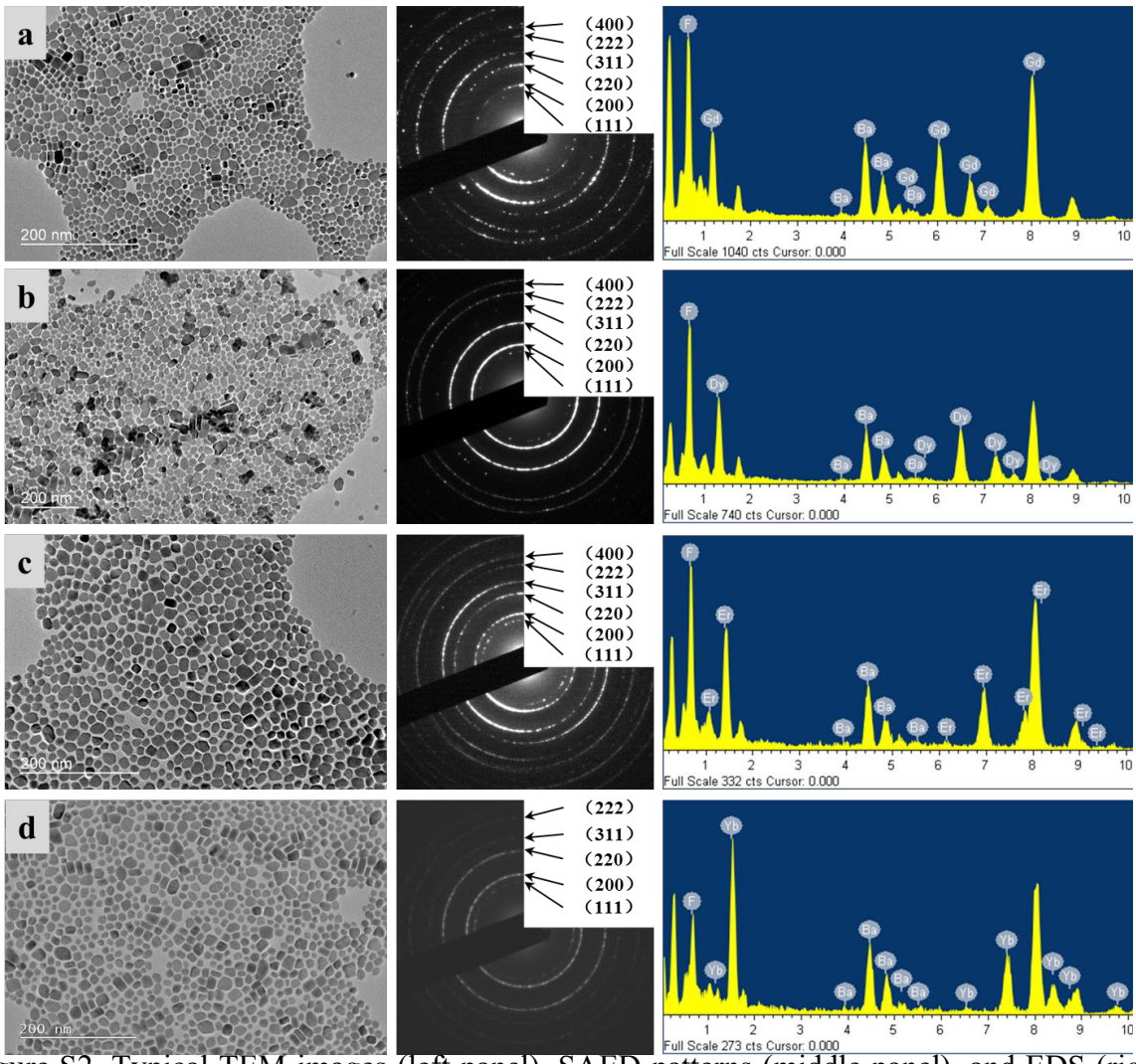

Figure S2. Typical TEM images (left panel), SAED patterns (middle panel), and EDS (right panel) of (a) pure $BaGdF_5$ NPs, (b) pure $BaDyF_5$ NPs, (c) pure $BaErF_5$ NPs, (d) pure $BaYbF_5$ NPs, respectively.

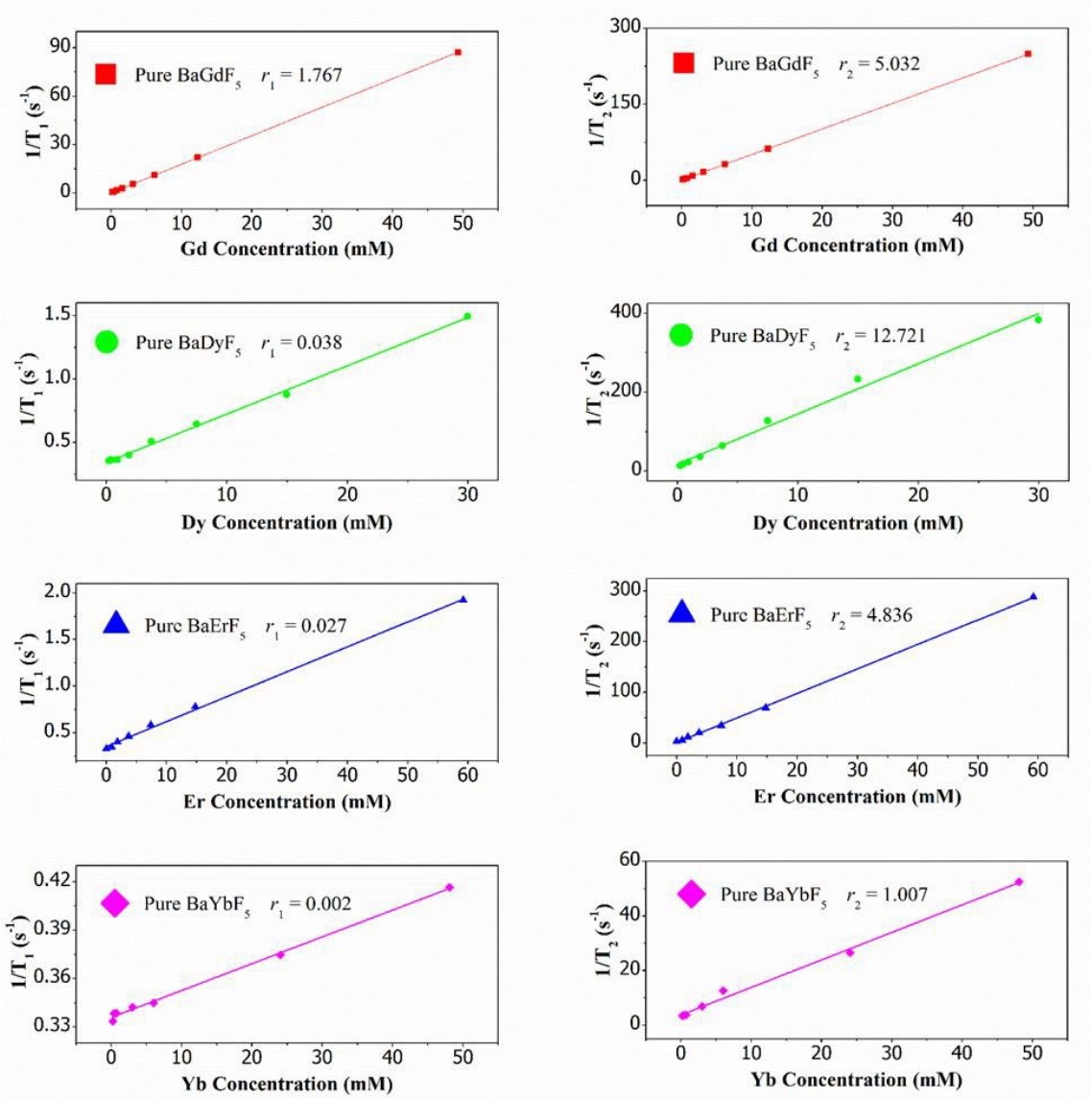

Figure S3. T_1 relaxivity time (left panel) and T_2 relaxivity time (right panel) measurements of (a) pure $BaGdF_5$ NPs, (b) pure $BaDyF_5$ NPs, (c) pure $BaErF_5$ NPs, (d) pure $BaYbF_5$ NPs, respectively, using a 1.5 T MRI scanner.

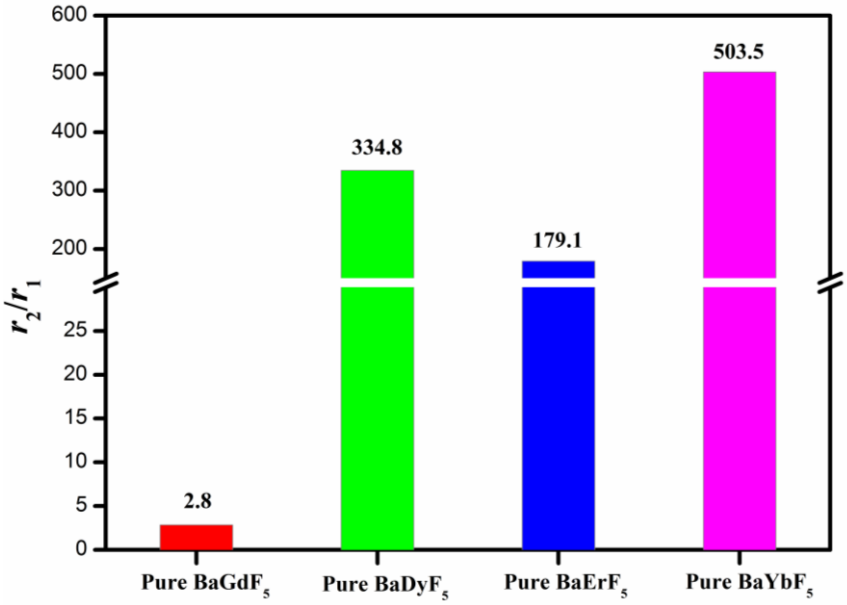

Figure S4. The calculated r_2/r_1 values of pure $BaGdF_5$, $BaDyF_5$, $BaErF_5$, and $BaYbF_5$ NPs, respectively.

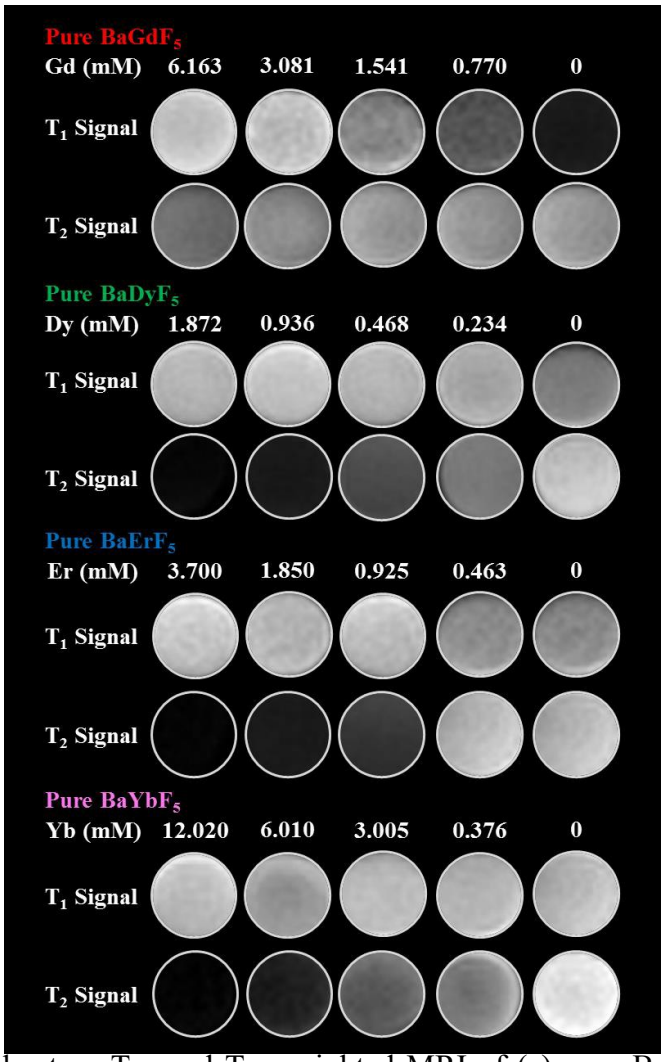

Figure S5. In vitro phantom T_1- and T_2- weighted MRI of (a) pure $BaGdF_5$ NPs, (b) pure $BaDyF_5$ NPs, (c) pure $BaErF_5$ NPs, (d) pure $BaYbF_5$ NPs, respectively.

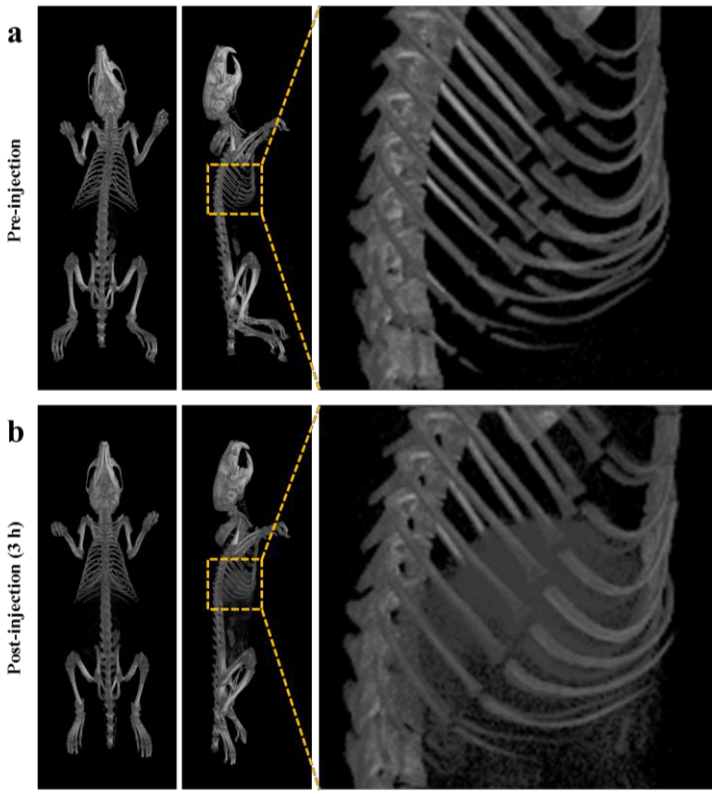

Figure S6. *In vivo* CT bioimaging of a mouse using BaGd/ErF_5 NPs as contrast agents via intravenous injection from tail vein.